Retinal organoids on-a-chip: a 3D printed micro-millifluidic bioreactor for long-term retinal organoid maintenance

Authors:

Yuntian Xue[1], Magdalene J. Seiler[4,2,3,7], William C. Tang[1], Jasmine Y. Wang[6], Andrew W. Browne[1,3,5]

Affiliation:

1. University of California, Irvine; Biomedical Engineering; Irvine CA
2. University of California, Irvine; Stem Cell Research Center; Irvine CA
3. University of California, Irvine, Gavin Herbert Eye Institute Department of Ophthalmology; Irvine CA
4. University of California, Irvine; Physical Medicine & Rehabilitation; Irvine, CA
5. University of California, Irvine; Institute for Clinical and Translational Science; Irvine, CA
6. University of California, Irvine; School of Biological Sciences; Irvine, CA
7. University of California, Irvine, Anatomy & Neurobiology, Irvine, CA

Corresponding Author:

Andrew W. Browne, MD, PhD, abrowne1@hs.uci.edu

Grant support:

California Institute of Regenerative Medicine (CIRM) grant number TRAN1-10995

RPB unrestricted grant to UCI Department of Ophthalmology

ICTS KL2 Grant number is KL2 TR001416

ABSTRACT:

Retinal degeneration is a leading cause of vision impairment and blindness worldwide and medical care for advanced disease does not exist. Stem cell-derived retinal organoids (RtOgs) became an emerging tool for tissue replacement therapy. However, existing RtOg production methods are highly heterogeneous. Controlled and predictable methodology and tools are needed to standardize RtOg production and maintenance. In this study, we designed a shear stress-free micro-millifluidic bioreactor. We used a stereolithography (SLA) 3D printer to fabricate a mold from which Polydimethylsiloxane (PDMS) was cast. The multi-chamber bioreactor design and fabrications methods easily combined micro and millimeter features with very low cost and short manufacturing time. We optimized the chip design using in silico simulations and in vitro evaluation to optimize mass transfer efficiency and concentration uniformity in each culture chamber. We successfully cultured RtOgs on an optimized bioreactor chip for 37 days. We also characterized the RtOgs produced by static dish culture and chip culture methods using qualitative and quantitative techniques. Phase contrast imaging showed that both conventional and chip-cultured RtOgs developed a transparent outermost surface structure. Fluorescence lifetime imaging (FLIM) showed that RtOgs on the chip had significantly lower long lifetime species (LLS) ratio than static cultured ones, which demonstrated that bioreactor cultured RtOgs exhibited less oxidative stress. RtOgs in bioreactor culture demonstrated higher NADH signal overall, but both bioreactor and conventional cultures showed similar free/bound NADH ratio over time, which indicated normal differentiation time course. RtOg gene expression was examined by fluorescence imaging and quantitative polymerase chain reaction (qPCR) analyses. RtOgs in both groups showed thick nuclear outer layers expressing CRX on day 120 of differentiation. The gene profiling showed both groups expressed retinal progenitor genes and most of the tested photoreceptor markers. We, therefore, validated an autonomous micro-millifluidic device with significantly reduced shear stress and lower oxidative stress to produce RtOgs of equal or greater quality than those maintained in conventional static culture.

Key words: Retinal organoids; Microfluidics; Millifluidics; 3D printing; Fluorescence lifetime imaging; Phasor approach; Functional imaging.

INTRODUCTION:

Retinal degeneration (RD) is a leading cause of vision impairment and blindness worldwide. Visual degeneration can originate in any of the cell types in the retina. Some of the more common visual degenerations stemmed from death and/or dysfunction of the photoreceptors (PR) and retinal pigmented epithelial (RPE) cells**.** These irreversible cell damages lead to vision loss manifested in age-related macular degeneration (AMD) and retinitis pigmentosa (RP). Retinal sheets and dissociated retinal cells are candidates for retinal tissue replacement therapy. However, both tissue sources have inherent limitations. Historically, retinal sheets derived from fetal neurosensory retina and RPE transplanted into the subretinal space demonstrated utility to restore vision and neurosensory functions [1-7] in animals [8-10] and humans [11]. However, the use of fetal tissue carried complex social, ethical, and political implications. Transplantation of dissociated photoreceptor precursors overcame the ethical issues and demonstrated some visual function improvements [12, 13] but dissociated cells introduced additional challenges [14-17] that mainly resulted from insufficient cell type differentiation, polarization and eventual cell death.

With the advent of human embryonic (hESCs) [18] and induced pluripotent stem cells (iPSCs) [19], stem cell-derived retinal organoids (RtOgs) have emerged as tools that exhibit the combined advantages of retinal sheets and differentiated retinal cells. RtOgs are 3D spheroid tissues that self-organized into layered retinal tissues containing retinal ganglion cells, rods and cones [20-22]. Transplantation of RtOgs have been shown to restore vision in retina degenerated rats [23], mouse [24] and primate [25] models with RD. Even so, the current state-of-the-art RtOg production methods are highly heterogeneous due to their use of different cell lines, culturing times, culturing methods, manual labor and imprecise tissue selections [26]. A comparative study revealed that RtOgs differentiated from iPSCs showed stage specific, cell line and methodological differences [27]. This heterogeneity and imprecision limit human RtOg procurement for preclinical trials [26] and *in vitro* investigations. Many approaches, including bioreactors [28-34] and optimized production protocols [26, 35] are investigated to standardize RtOg production and maintenance over months. Controlled

and predictable RtOg production is important to ensure a quality-controlled tissue product that is suitable for transplantation.

In recent years, many *in vitro* cell culture platforms have emerged for organoid differentiation and maintenance at the macro-, milli-, and microscales. Macro-scaled platforms are typically utilized for their ease and effectiveness in producing organoids, while milli-scaled systems (≥ 1 mm) are employed for relatively high flow rates, cell-cell interaction, and less frequent media changes and thus less organoid perturbation and lower probability for damage [29]. Considering the costs associated with the relatively high media volumes required by the macro-scaled bioreactors, microscale devices (< 100 μm) are steadily growing in popularity [36]. Microfluidic devices shared the advantages of millifluidic devices, with the further advantage of even lower media consumption. However, the dimensional limits of traditionally fabricated microfluidics devices hinder its application to organoids research since organoids are 3D spherical tissues that can grow up to several millimeters in size. Fig. 1 summarizes current published organoid bioreactors and their advantages and disadvantages. The integration of micro- and millifluidic device is a promising solution for organoids differentiation and maintenance.

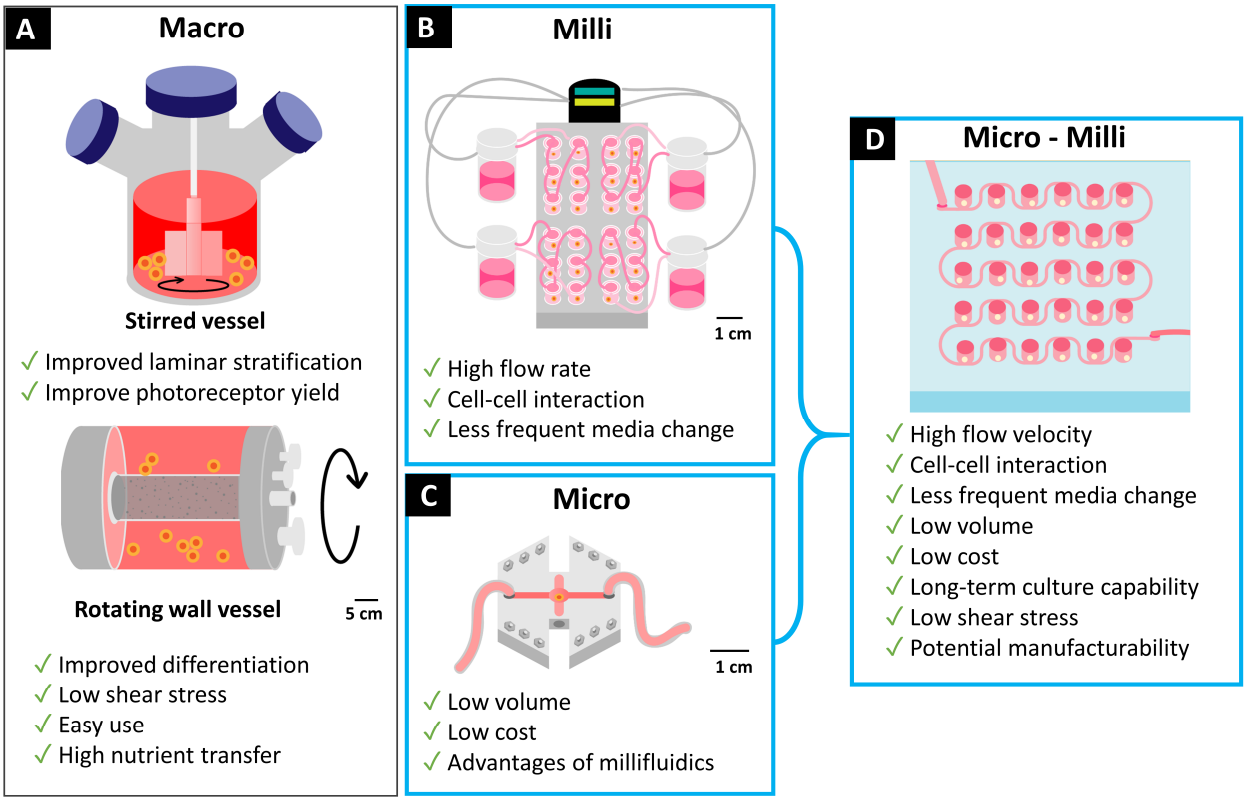

Figure 1: Review of Organoid Bioreactors. (A) Macro scale bioreactors: stirred/spinning and rotating wall vessels [37]; (B) Millifluidic bioreactor [38]; (C) Microfluidic bioreactor [39]; (D) Micro-millifluidic bioreactor in this article.

In this study, we designed and fabricated a shear stress-free micro-millifluidic bioreactor for use in RtOg culture and maintenance. We used a high resolution (25 μm) stereolithography (SLA) 3D printer to fabricate the mold for Polydimethylsiloxane (PDMS) molding, which easily combined micro and millimeter features in one design with very low cost and short manufacturing time. First, we simulated the fluidic design parameters in COMSOL to optimize the fluidic transports in the chip design. We evaluated 3 different factors that could affect mass transfer efficiency and uniformity. We then successfully cultured RtOgs on the designed chip platform for more than one month (37 days). Finally, we did a comparative study to characterize the RtOgs produced by dish culture (denoted as “static” because there was no constant media flow through the dish) and chip culture. We compared live organoids both qualitatively and quantitatively.

METHODS

COMSOL simulation

The simulation was performed using finite element analysis software, COMSOL Multiphysics (COMSOL, Inc, Palo Alto, CA, USA). COMSOL was used to evaluate different chip designs and flow channel configurations to optimize mass-transport dynamics in culture chambers with different heights. Three major factors that affected the mass transfer rate were taken into consideration: 1) channel width (1000 or 500 μm wide), 2) channel configuration relative to culture chambers (linear single-sided chambers, serpentine alternating side chambers, serpentine with integrated mixer) and 3) the culture chamber height (2 or 4 mm tall).

The simulation parameters are listed in Table 1. The initial concentration of the whole system was set to zero, which was considered the most extreme condition. The left end of the channel was set as the inlet with concentration of 1 mol/m^3 as the boundary condition.

Table 1: Simulation parameters

Physics	Laminar flow & Transport of diluted species
Study type	Time dependent
Material	Water
Diffusion coefficient (m^2/s)	6.00E-10
Boundary conditions (mol/m^3)	$c_{initial} = 0$, $c_{inlet} = 1$

Chip design and fabrication

The mold was designed using SolidWorks (SolidWorks Corp., Waltham, MA, USA) and the final design used for RtOg culture had the dimensions shown in Fig. 2A with channel height of 200 μm and chamber height of 2 mm. The chambers were arranged in a 6 x 5 array with the

distance between each chamber at 9 mm, which was the same as that of a 96-well plate for compatibility with subsequent imaging steps. The mold was produced with 25 μm resolution with the Formlabs Form 3B printer (Formlabs, Somerville, MA, USA) using standard clear resin (Formlabs) (Fig. 2B). After printing, the mold was cleaned with 90% isopropanol to remove any resin residue. The mold was then air dried for 24 hours and cured with ultraviolet light for 30 minutes.

The bioreactor was fabricated from the printed mold similar to the molding steps in soft lithography [40]. Polydimethylsiloxane (PDMS) Sylgard 184 (Dow Corning, Midland, MI, USA) was mixed manually for 10 minutes at a 10:1 ratio (base elastomer/curing agent). After degassing in a vacuum chamber, the PDMS was poured over the 3D-printed mold until the level reached the top of the culture chamber features and degassed again in a vacuum desiccator to remove bubbles (Fig. 2C). After 48 hours of curing under room temperature, the molded PDMS piece was carefully peeled off from the mold. The fluidic inlet and outlet were created with a biopsy punch. Finally, the PDMS piece was treated with air plasma (Harrick) (Harrick Plasma, Ithaca, NY, USA) for 1 min. to promote adhesion and then pressure-bonded to a cover slip (#1.5, 64*50 mm, ClariTex) (Ted Pella, Inc., Redding, CA, USA) (Fig. 2D).

Stem cell culture and retinal organoids initiation

Retinal organoids were differentiated from genetically modified registered human embryonic stem cells (hESCs) with green fluorescent protein (GFP) tagged to CRX gene which encodes cone-rod homeobox protein and is specifically expressed in photoreceptor cells (WA01 line expressing CRX-GFP) [41]. Stem cells were maintained by feeding mTeSR 1 media (STEMCELL Technologies, Vancouver, BC, Canada) daily and passaged every 4-7 days by ReLeSR (STEMCELL Technologies) when cells reached ~80% confluency. Cells were expanded on Vitronectin XF™ (STEMCELL Technologies) coated plates at 37 °C in a humidified 5% CO_2 incubator (Nuaire, Plymouth, MN, USA).

To initiate organoid formation, Accutase (Nacalai Inc, Kyoto, Japan) was added to the stem cells into a single cell suspension when 2-dimensional culture reached ~80% confluency. The cells were then placed in a 800-μm micro-well EZSPHERE 12-well plate (Nacalai) and centrifuged at 100*g* for 3 min. to evenly distribute the stem cells throughout the bottom of each well. From day 1 to 7, the stem cells self-aggregated into embryonic bodies (EBs) in the EZSPHERE microwells. From day 8, the EBs were seeded onto a 1% growth factor reduced Matrigel (r) coated culture dish. The EBs spread onto the Matrigel and began 2D differentiation. Retinal eye fields were cut from the Matrigel on day 50 and transferred to ultra-low attachment 24-well plates (Corning Costar) (Corning, Corning, NY, USA) for 3D culture to be loaded into the bioreactor chip. Media used for retinal organoid differentiation was modified from Zhong *et al*. [42] From day 0 to 18, the organoids were gradually transitioned from mTeSR1 medium into neural induction media (NIM) containing Dulbecco's modified eagle medium (DMEM)/F12 (1:1), 1% N2 supplement (Gibco™) (Thermo Fisher Scientific, Waltham, MA, USA), 1x minimum essential media non-essential amino acids (NEAA) (STEMCELL Technologies), 1x L-glutamine (STEMCELL Technologies), and 2 μg/ml heparin (Sigma-Aldrich, St. Louis, MO, USA), with daily media changes. From day 19 to 41, the media was switched to NIM containing DMEM/F12 (1:1) supplemented with 2% B27 supplement (without vitamin A, Gibco), 1x NEAA, 1x L-glutamine, and 2mg/ml heparin. From day 42 and beyond, the organoids were cultured with media containing DMEM/F12 (1:1) supplemented with 2% B27 supplement (Gibco), 1x NEAA, 1x L-glutamine, 2ug/ml heparin, 100 μM taurine (Sigma), and 10% fetal bovine serum (FBS; Gibco). The media was changed 3 times a week and the organoids were maintained at 37 °C in a humidified 5% CO_2 incubator.

The organoids used in this study were all generated from the same batch. On day 87 of differentiation, 15 RtOgs were randomly selected to load one each into every other chamber in the bioreactor chip. After 37 days of on-chip culture, 3 RtOgs were selected for histology. The remaining 12 RtOgs were divided into 3 groups of 4 RtOgs for qPCR gene expression analysis.

Bioreactor system assembly and organoid loading

The chip and the associated tubing were disinfected with 70% ethanol and 30 min. in a UV and ozone cool clave (CoolCLAVE Plus) (Genlantis, San Diego, CA, USA). Each chamber was treated with anti-cell adherence solution twice (STEMCELL Technology) and washed by Dulbecco's phosphate-buffered saline (DPBS) without calcium and magnesium (STEMCELL Technology). The on-chip culturing system was assembled as shown in Fig. 2F. The media reservoir was comprised of a 50 mL Steriflip-GP sterile centrifuge tube (MilliporeSigma, Burlington, MA, USA) and a filter cap with a pore size of 0.22 μm.

Before loading the organoids, the chip chambers were sealed by pasting a slice of MicroAmp™ optical adhesive film (Thermo Fisher Scientific, Waltham, MA, USA) on the top surface, then slowly withdrawing the syringe to apply negative pressure to fill the channel with fresh media drawn from the media reservoir. Tubing clamps were then applied to block both the inlet and outlet tubing, so that the adhesive film could be removed without disturbing the fresh media level in the channel. One organoid was loaded into each chamber by 20 μL pipette tips with tip heads cut off. Lastly, the top of the chambers was resealed with sterile optical adhesive film (Fig. 2E). The flow rate used for long-term culture was 250 μL/h. Under this flow rate, 50 mL media was sufficient for about 8 days of culture. When changing the media, the inlet and outlet tubing were clamped and fresh media was refilled in the centrifuge tube. All these steps were performed in an ESCO Class II Type A2 biosafety cabinet (Labculture, ESCO) (ESCO Micro Pte. Ltd., Singapore) to avoid contamination.

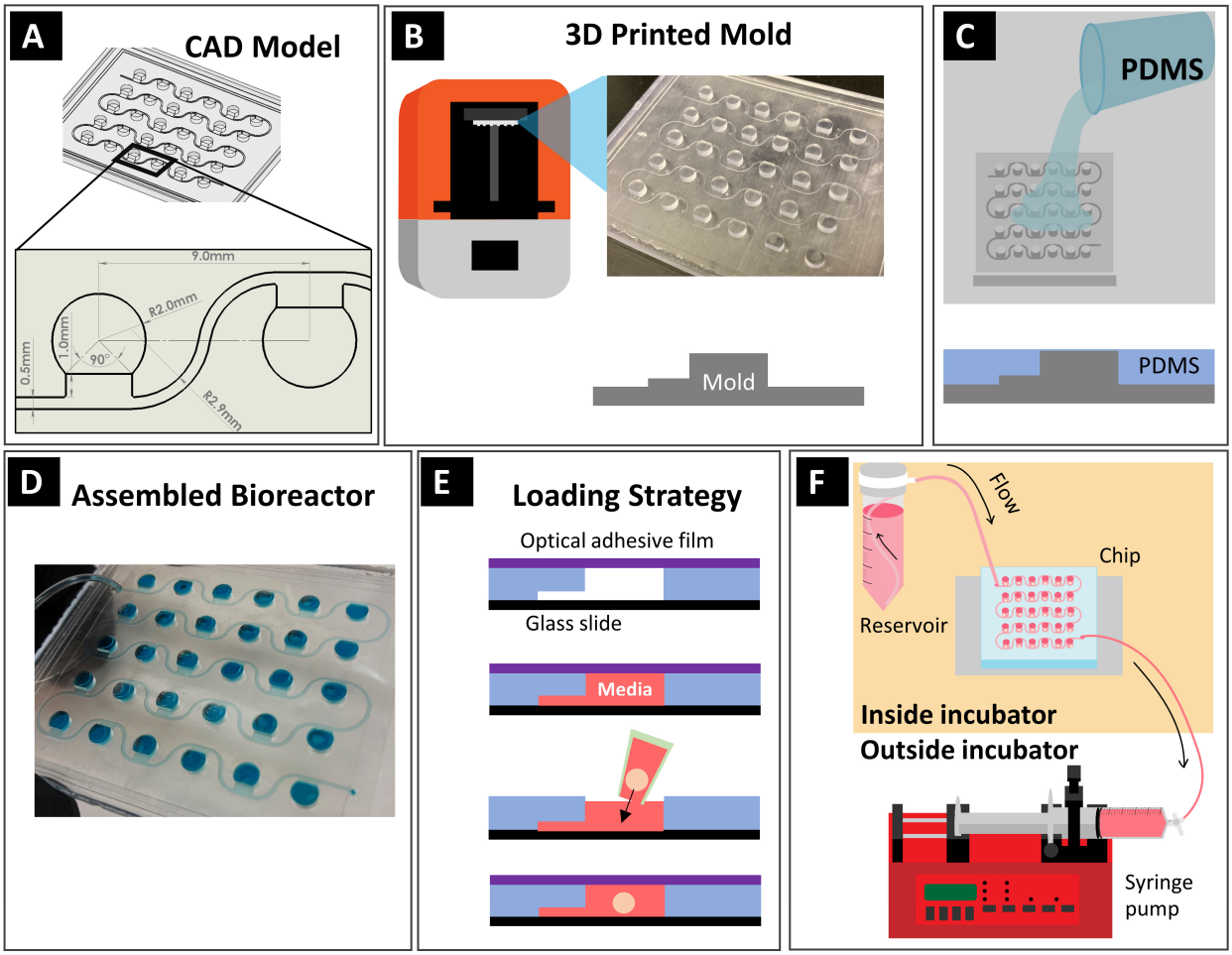

Figure 2: Fabrication methods. (A) Mold design with CAD software; (B) Mold printing; (C) PDMS casting on the mold; (D) Assembled bioreactor; (E) Cross section view of organoid loading procedure whereby microchannels were filled with media first, then an organoid was placed in the open well, and the wells were sealed using adhesive optical film; (F) On-chip culturing system assembly.

In vitro dye test

The dye test experiment was performed to compare the uniformity of the concentration in chambers between the four different channel designs. Four chips with 3x3 chamber array were fabricated with 2-mm chamber height. The channels were first filled with blue food dye solution following similar steps as the organoid loading procedure (Fig. 2E). The flow was then blocked by clamping both the inlet and outlet tubing, and the inlet was switched to a yellow dye solution.

Lastly, a syringe pump was used to draw the yellow dye solution into the chip at a rate of 600 μL/h. The whole flow process was recorded with a camera. The grayscale value of each chamber was obtained by ImageJ to quantify concentration changes of each chamber from the images.

Fluorescence life-time imaging

Fluorescence lifetime imaging (FLIM) was used to study the intrinsic fluorophore Nicotinamide adenine dinucleotide (NADH) in the RtOg. The fluorophore's emission decay curve was obtained by photon counting to calculate the fluorescent lifetime (Fig. 3A). FLIM data was displayed on a phasor plot after Fourier transform, with the intensity decay curve of fluorescence for each pixel represented by the *g* and *s* coordinates. Using this method, the decay and spectrum for each pixel could be depicted on the phasor plot (Fig. 3B).

The metabolic trajectory was visualized with phasor approach [43]. The phasor plot has a universal circle, with boundaries of each point representing a single exponential lifetime of one type of molecule. Different components on the phasor plot followed a linear relationship, thus, the ratio of the linear combination could be used to determine the fraction of each component. The lifetime of free and lactate dehydrogenase-bound NADH was about 0.37 ns and 3.4 ns, respectively [44]. Free NADH was linked to more glycolysis and a more proliferative state, while bound NADH was correlated with more oxidative phosphorylation and a more differentiated state [45]. The lifetime of lipid was 7.89 ns associated with long lifetime species (LLS) (Fig. 3B), the presence of which indicated oxidative stress [46]. The fraction of each component was calculated as Fig. 3B suggested, F1/F2 was the free/bound NADH ratio, and F3 was the ratio of LLS. Based on the above mechanism, we evaluated the metabolic state of RtOgs quantitatively by calculating the free/bound NADH ratio and LLS ratio in representative image cross-sections. Qualitatively, the metabolic differences were visualized by applying a pseudo color gradient to the phasor plot (Fig. 3C).

Images were taken by Zeiss LSM 780 microscope using a Plan-Apochromat 20x/0.8 M27 objective (Carl Zeiss, Jena, Germany). The excitation wavelength was 740 nm, produced by Mai Tai multi-photon laser source (Spectra-Physics Mai Tai, Mountain View, CA). Imaging settings used were as follow: 256 x 256 frame size, 1.66 µm pixel size, 25.21 µs pixel dwell time and 8 bit pixel depth. Emission laser passed through an MBS 690+ and an SBS SP 610 filters and the lifetime data was collected by the photomultiplier tube (H7422p-40, Hamamatsu, Japan) and a320 FastFLIM FLIMbox (ISS, Champaign, IL). Before imaging, the system was calibrated on frequency factor and lifetime by coumarin 6 solution with the known lifetime of 2.5ns. FLIM data were collected after 100 counts in the brightest pixel of the image were acquired.

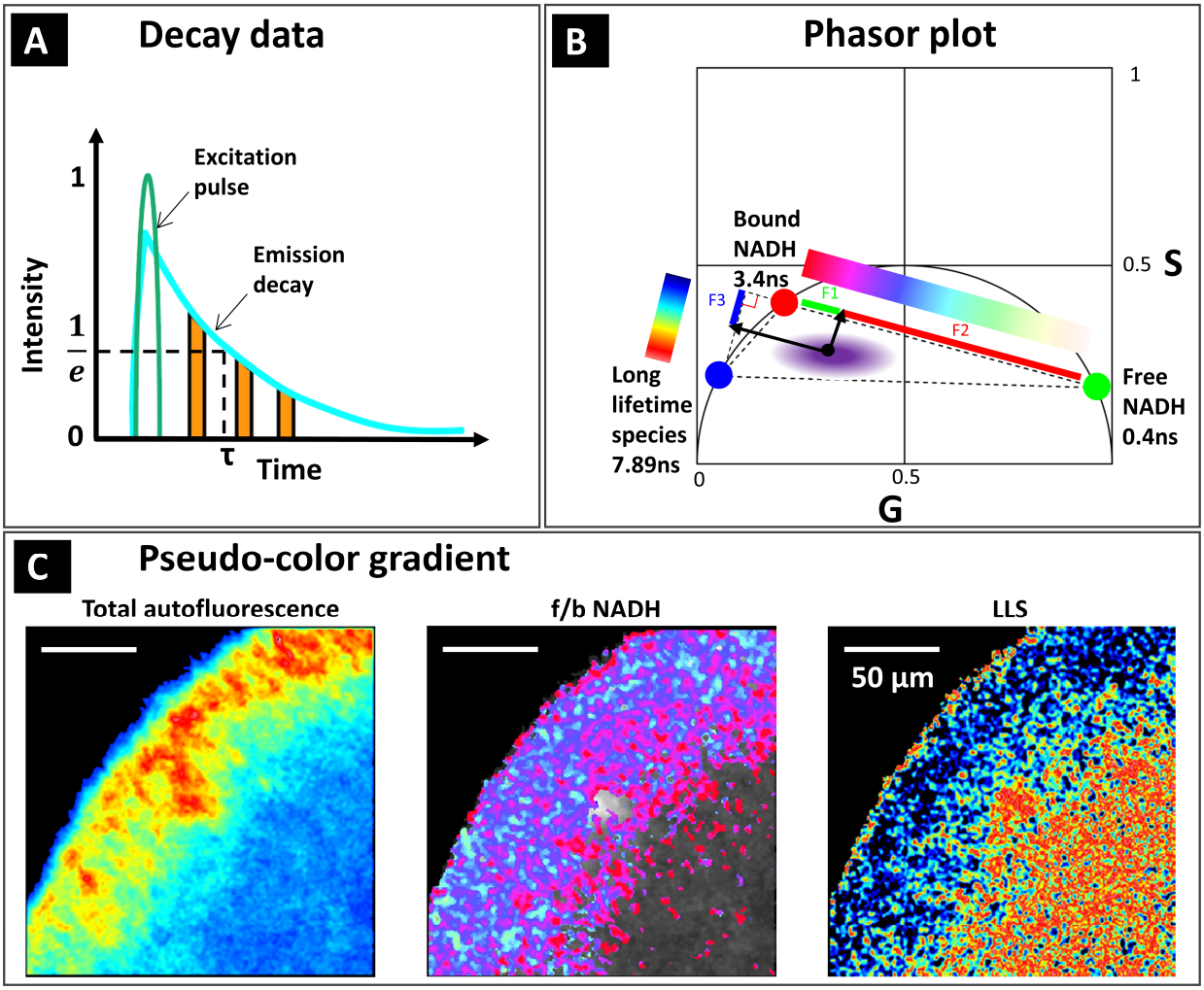

Figure 3: Fluorescence lifetime imaging and analysis using the phasor approach. (A) Fluorescence lifetime was acquired by quantifying emitted fluorescent photon over time after an excitation pulse was supplied to obtain an emission decay curve; (B) Phasor plot produced a 2-dimensional space for intrinsic fluorophors with different lifetimes corresponding with different types of metabolism (oxidative phosphorylation favors bound NADH and glycolysis favors free NADH) and different amounts of oxidative sress (long lifetime species). The free/bound NADH ratio and long LLS ratio were obtained by calculating projecting the 3 dimensional photon count histogram onto the Bound-Free axis and LLS axis respectively; (C) A representative images of RtOg analyzed by the phasor approach. The autofluorescence images encapsulated all total fluorescenee, while the f/b NADH and LLS are pseudocolor images based on the phasor analysis of quantized fluorescent emission. f/b NADH was free to bound NADH ratio. LLS was long lifetime species.

Phase contrast imaging

The phase contrast microscopy images were acquired using an Olympus IX71 (Olympus, Tokyo, Japan) and a QICAM FAST1394 CCD camera (Teledyne QImaging, Surrey, BC, Canada) under two magnifications by UPlanFL N 4x/0.13 PhL and UPlanFI 10x/0.30 PhL objectives.

Green fluorescent protein imaging

Green fluorescent protein images were acquired using a Zeiss LSM 780 microscope using Plan-Apochromat 20x/0.8 M27 objective (Carl Zeiss, Jena, Germany). The excitation wavelength was 488nm with a pixel dwell time of 1.58 μs. We used the frame size of 512 x 512 pixels and each pixel is 0.42 μm.

Quantitative polymerase chain reaction analysis

The primers for qPCR test were listed in Table S1 (Qiagen, Germantown, MD, USA). We used 12 retinal progenitor and photoreceptor genes and 1 housekeeping gene to identify and

quantify the gene expression profile in retinal organoids. Human adult retinal tissue was used as a positive control (n = 3). Each RtOg sample was analyzed at days 122 to 124 of differentiation (n = 3 for both static and chip groups). Each sample consisted of 4 individual RtOgs. Trizol reagent (Qiagen), DNase I digestion (Fisher, Waltham, MA, USA), and phenol-chloroform extraction (Fisher) were used to isolate RNA, and an RT^2 cDNA synthesis kit (Qiagen) was used to synthesize cDNA. RT^2 SYBR Green with ROX qPCR master mix (Qiagen) was used for amplification, which was performed under the following conditions: 95°C (15 minutes), 40 cycles at 95°C (15 seconds each), 55°C (30 seconds each) and 72°C (30 seconds each). The annealing temperature was 60°C. The double delta cycle threshold (Ct) method was used to calculate the fold expression, and day 0 undifferentiated hESC (line CSC14) was used as a control. For the purpose of analysis and heatmap generation, non-detected amplification in the control tissue and organoids were assigned cycle threshold values of 40. Heat maps were generated using Graphpad Prism software (Graphpad Software LLC, La Jolla, CA, USA), the heat map has the value of $\log_2(\text{Fold Expression})$, which is equal to $-\Delta\Delta C_t$.

Histology and hematoxylin-eosin staining

RtOgs at day 124 of differentiation were fixed with cold 4% paraformaldehyde in 0.1M Na-phosphate buffer for 1 hour (static: n = 2; bioreactor: n = 3), cryoprotected (30% sucrose) and frozen in optimal cutting temperature compound. Cryostat sections (10 µm) were stored at –20°C. Slides in both groups were stained using hematoxylin and eosin and then imaged on an Olympus BXH10 (Center Valley, PA, USA) using an Infinity 3-1U camera (Lumenera, Ottawa, Ontario, Canada).

Statistical analysis

Data in the plot were presented as means with standard deviations. Graphpad Prism software was used for all statistical analyses. In the GFP MFI, free/bound NADH and LLS ratio figures,

one-way ANOVA test was performed. In the qPCR heatmap, two-way ANOVA test was performed. The significance was determined by a *p* value less than 0.05.

RESULTS

Microfluidics design and testing

The chip design was a miniature version of a conventional tissue culture plate with the distance between chambers matching a 96-well plate to retain microscope compatibility. Preliminary designs in which chambers were located on one side of a 1000 μm wide perfusion channel revealed two problems: 1) uneven concentration among chambers and 2) low mass transfer efficiency (Fig. S1). Therefore, not all wells in the preliminary design received comparable media perfusion. To optimize the design, three different variables that affected the mass transfer rate were evaluated with COMSOL simulation: channel width, channel alignment and chamber height.

The channel width determined the cross-section area and thus affected the flow velocity (*v*) as indicated in Equation (1). Holding volume flow rate (*Q*) constant, the larger the cross-sectional area (*A*), the slower the flow velocity (*v*) would be.

$$Q = Av \tag{1}$$

According to the definition of Péclet number (Pe_L, the ratio of advective transport rate to diffusive transport rate, Equation (2)), larger flow rate would lead to higher advective transport rate, accelerating mass transports.

$$Pe_L = \frac{Lv}{D} \tag{2}$$

where *L* is the characteristic length, *v* the local flow velocity, and *D* the mass diffusion coefficient. Therefore, narrowing the channel width would facilitate an increase in flow velocity. Based on the simulation results, under both flow rates, the narrow channel (500 μm) designs

showed faster mass transfer (Figs. 4A-B) and therefore, a theoretically faster delivery of media to each culture chamber.

Incompressible fluid flow within the microfluidic device, due to its small size, should be laminar with a parabolic velocity profile when fully developed. As a result, the velocity next to the channel walls should be close to zero. Thus, the designs with all chambers on one side of each channel should show a higher velocity in the fluid close to the channel wall connected to a chamber and that on the opposite wall. Figs. 4A-B show that single-sided channel showed a concentration gradient from the first chamber to the last chamber in each row and then entire series of chambers. This difference was even more pronounced in larger series of 5 x 6 chambers (SFig. 1). To minimize this effect, a serpentine channel was designed to promote comparable media diffusion from both sides of the channel. To further improve concentration distribution, a mixer unit was added between each chamber [47]. Empirical evidence with a larger 5 x 6 array of organoids demonstrate significant variability between chambers in each row (SFig. 1). Simulation demonstrated that narrow channels with or without mixer showed comparable qualitative performance as indicated with the color map representation of the concentration variations between the first and last culture chambers in each row and those between rows.

The third variable evaluated with simulation was the chamber height. By tracking the point concentration on the same top corner of each chamber, the 3D COMSOL simulation results showed that doubling the height of the chamber to 4 mm caused a dramatic change (4~10 folds difference) in mass transport efficiency (Fig. 4D). To maximize the transport efficiency, we chose 2 mm as our final chamber height for bioreactor fabrication. Fig. 4E shows the 3D concentration patterns in four different bioreactor designs.

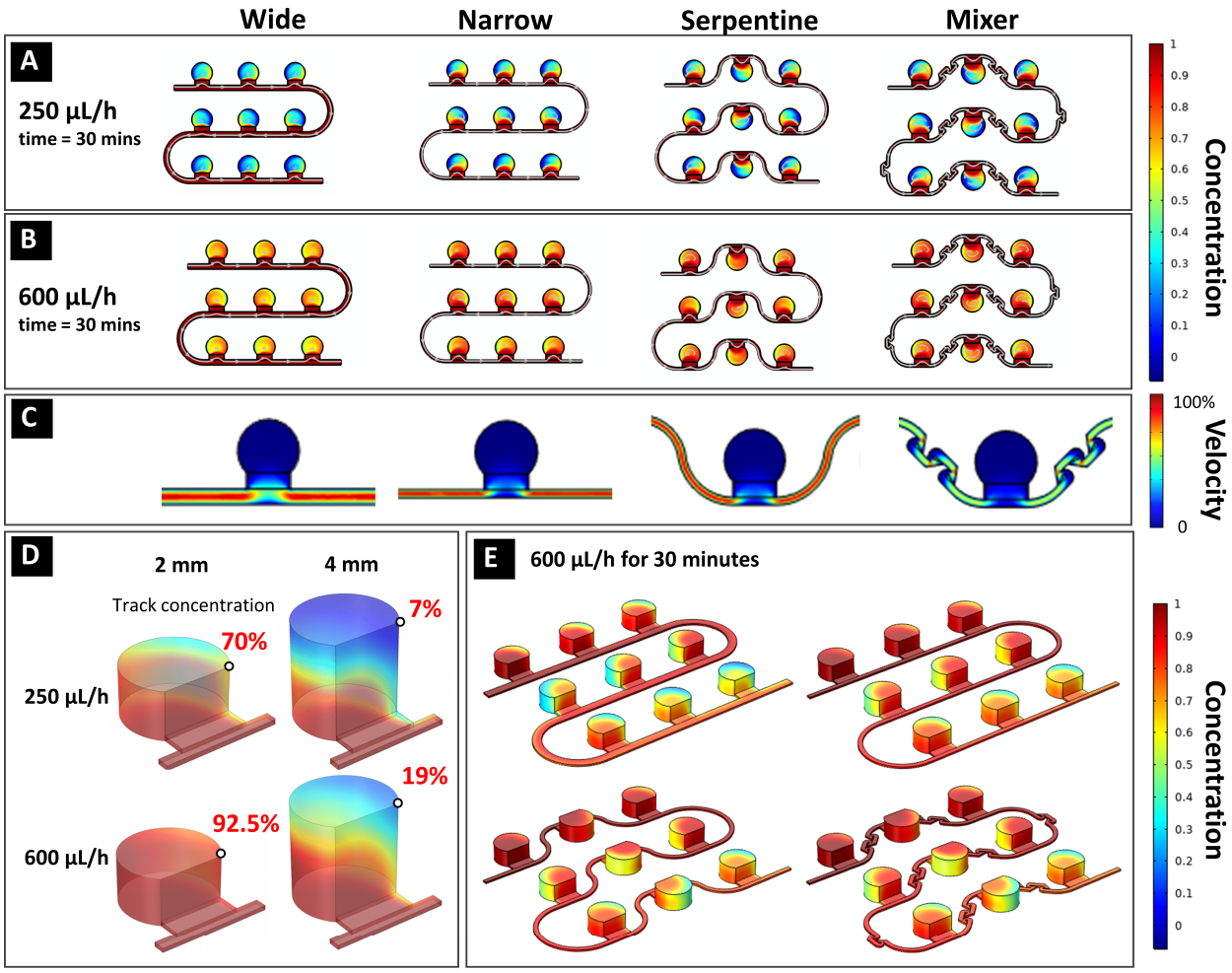

286

287 **Figure 4: COMSOL simulation of 4 different channel designs.** (A) Concentration distribution
288 after 30 minutes of slow flow (250 µL/h); (B) Concentration distribution after 30 minutes of fast
289 flow (600 µL/h); (C) Velocity distribution – zero velocity in all chamber demonstrated shear stress-
290 free culture environment. A single culture chamber and adjacent flow channels is shown because
291 focal flow velocity was identical for every culture chamber and interconnecting microfluidic
292 channels in the linear series; (D) Mass transfer efficiency comparison between different height
293 chambers under two different flow rates after 30 minutes. Black circles represent location of
294 concentration determination at 30 minutes; (E) 3D concentration pattern of four different designs.
295

296 To confirm simulation results and examine the functionalities of the four designs, a dye test
297 was performed to confirm the optimum design for culturing RtOgs. A 3 x 3 chamber array was
298 fabricated for each channel design with a 2 mm tall culture chamber. Blue dye was used to fill
299 each channel followed by 30 and 48 minutes of 600 µL/h flow of yellow dye (Fig. 5A). The
300 grayscale photogrammetry from pictures taken on each chamber were quantified (Fig. 5B). The
301 serpentine channel with mixer design showed the smallest standard deviation, indicating that this
302 design had the most uniform concentration among the four. The serpentine channel without mixer
303 exhibited the next best performance based on variability after 48 minutes of flow. The simple
304 serpentine channel without mixer showed higher fabrication success with 3D printing and lower
305 probability of trapped air bubbles in the microfluidic channels than the serpentine channels with
306 mixer.

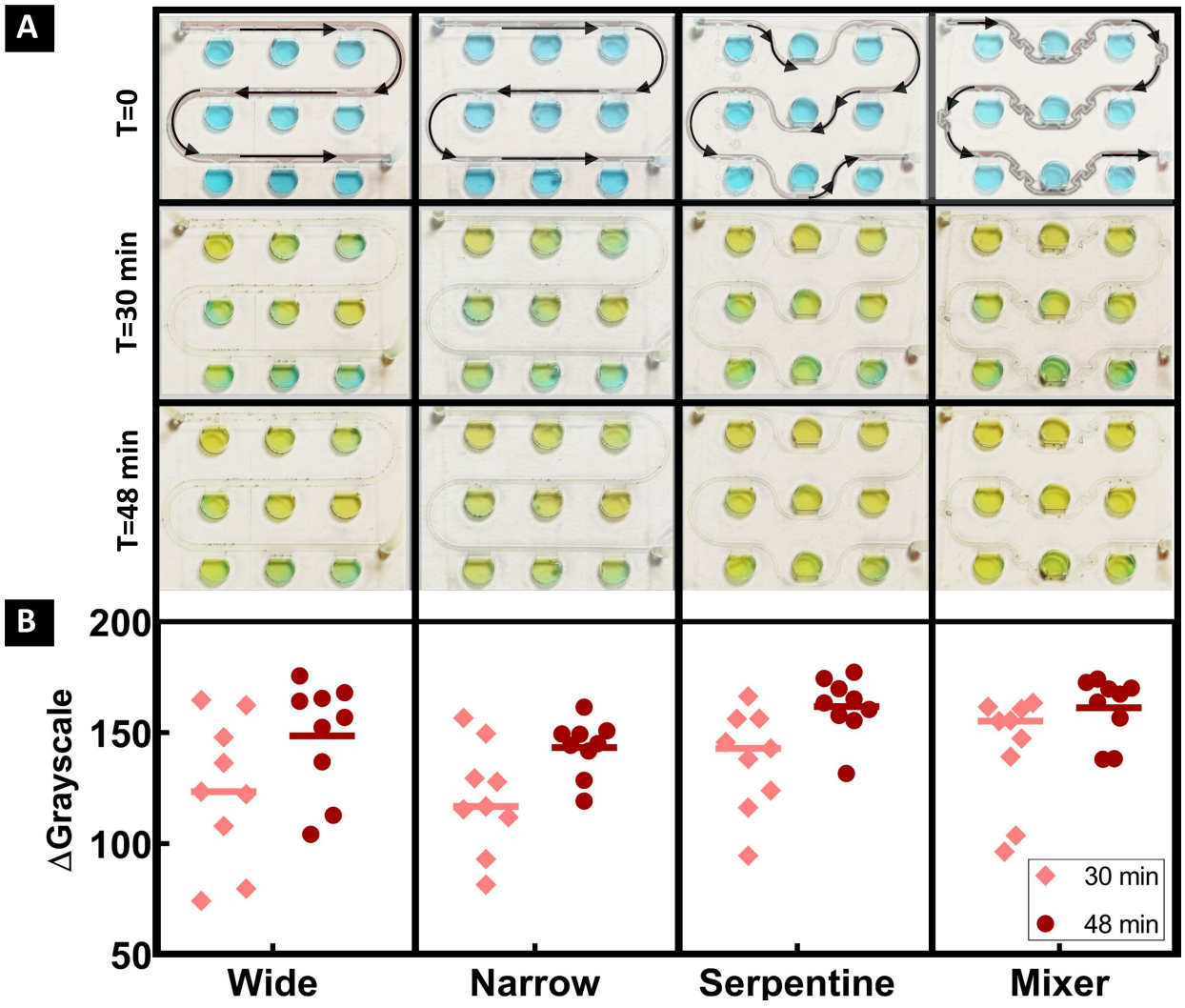

Figure 5: Flow and concentration distribution experiment with dye. (A) Diffusion pattern of four different designs (flow rate was 600 µL/h); (B) Grayscale change of each well after 30 minutes and 48 minutes.

Retinal organoid culture methods comparison

Phase contrast imaging

The RtOgs used in this study were differentiated from human embryonic stem cells. Representative phase contrast images in Figs. 6A-E showed the key stages of RtOg differentiation. The EZSPHERE microwell was used to form stem cells into uniformly sized embryonic bodies. Eye fields cut from Matrigel were maintained in ultra-low attachment 24-well

plate as they assembled into RtOgs. In this study, RtOgs were put on the bioreactor on day 87 of differentiation.

Figs. 6F-M showed two representative RtOgs in both groups on day 88 and day 124 of differentiation, respectively. The observable transparent and laminar outer surface, which was observed in both groups, indicated development of a photoreceptor layer. For the bioreactor culture method, the RtOgs tended to grow beside the chamber wall (Fig. 6I). The bioreactor was treated with anti-cell adherence solution twice (STEMCELL Technology) before introducing RtOgs, which effectively prevented adhesion during the first three weeks. However, after three weeks, some of the RtOgs began attaching to the chamber walls without extending along the PDMS surface. As a result, the RtOgs continued to undergo 3D differentiation albeit displaying slight deformation due to the physical contact with the chamber wall.

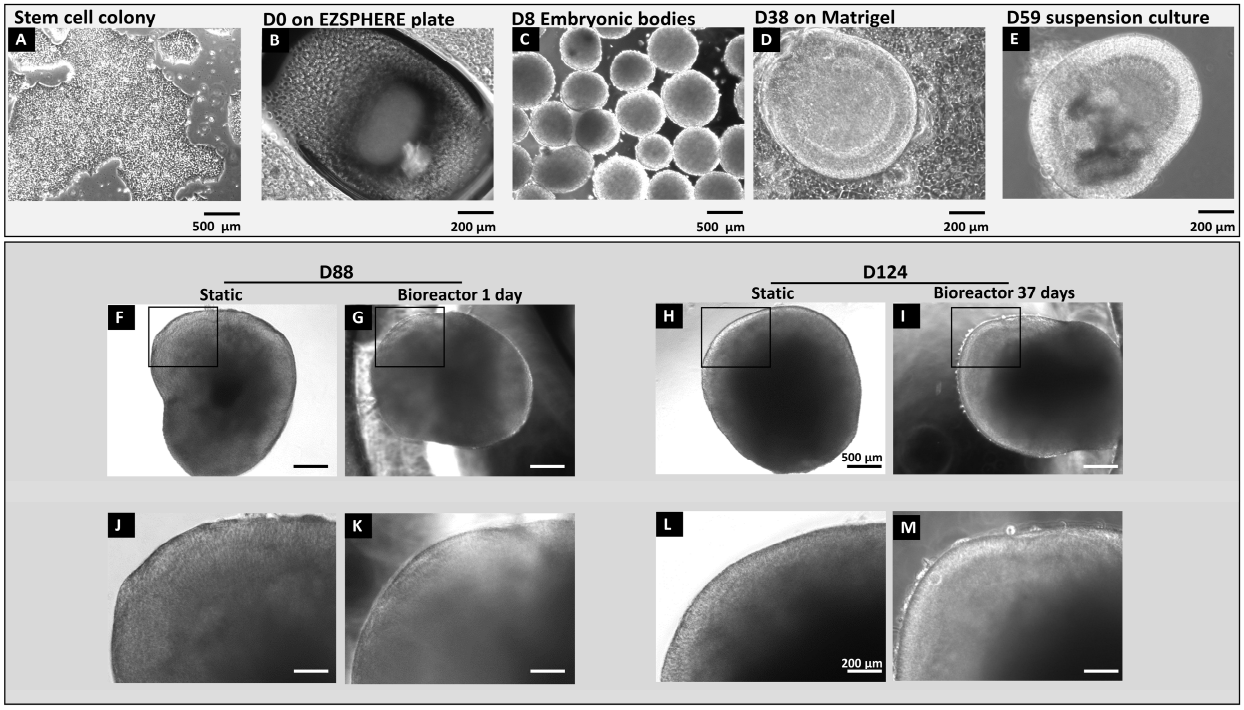

Figure 6: Phase contrast images. (A) Human embryonic stem cell colony; (B) Day 0 of differentiation, dissociated stem cells in EZSPHERE microwell plate (well size: 800 µm); (C) Day 8 of differentiation, embryonic bodies ready for seeding on Matrigel; (D) Day 38 differentiation on Matrigel; (E) Retinal organoid in suspension culture on day 59; (F-G) RtOgs on day 88 of

differentiation; (H-I) RtOgs on day 124 of differentiation; (J-M) Higher magnification images correspondeng to images above in F-I.

Fluorescence lifetime imaging

The bioreactor chip platform was supplied with nutrients continuously while the RtOgs in conventional dish culture received nutrient exchange every 3 days. This distinction might cause metabolic differences in the long-term. The hypothesis is that chip cultured RtOgs would experience less oxidative stress caused by reactive oxygen species (ROS), and the sufficient nutrients supply would benefit RtOgs survival and maturation. We previously used FLIM for live RtOg characterization [48]. FLIM was used to measure the metabolic activity in a non-invasive and non-destructive way as described in the method section.

Four imaging modalities were used to visualize the same cross-section in RtOgs. Conventional fluorescence microscopy demonstrated greenfluorescnt protein in photoreceptors and their progenitors (Figs. 7E-H). Multiphtoton infrared stimulation was used to acquire total autofluorescent images showing the total NADH (Figs. 7A-D), which delineated cellular structures and viability of RtOgs. Multiphoton lifetime imaging revealed metabolic changes in NADH from its free to bound form and their associated free:bound ratio (f/b NADH) (Figs. 7I-L). Long lifetime species analysis highlighted oxidative stresses in the tissues (Figs. 7M-P).

From day 98 to day 120 of differentiation, RtOgs in both groups shifted from more glycolytic (yellow-green) to more oxidative phosphorylation (red) (Figs. 7I-L), the difference was significant (Fig. 7S), which suggested that RtOgs on day 120 were more differentiated from a stem cell state (glycolytic) [49, 50]. Furthermore, greater metabolic signature from NADH was present from bioreactor cultured organoids (Comparing Figs. 7K and 7L). When compared within groups, the bioreactor cultured RtOgs had no significant different f/b NADH ratio on day 120 (Fig. 7S), which indicated that RtOgs in both groups obtained comparable differentiation states. The LLS images showed a distinct color difference between two groups (Figs. 7M-P). RtOgs on the bioreactor had experienced significantly lower oxidative stress than RtOgs in static culture at both imaged

timepoints, and both groups increased LLS ratio across days (Fig. 7T). The time-dependent metabolic shifts and the metabolic difference between two groups were also reflected on G-S phasor plot, which provided the metbolic fingerprint of each group of samples. The measured RtOgs were located at four different clusters (Fig. 7R).

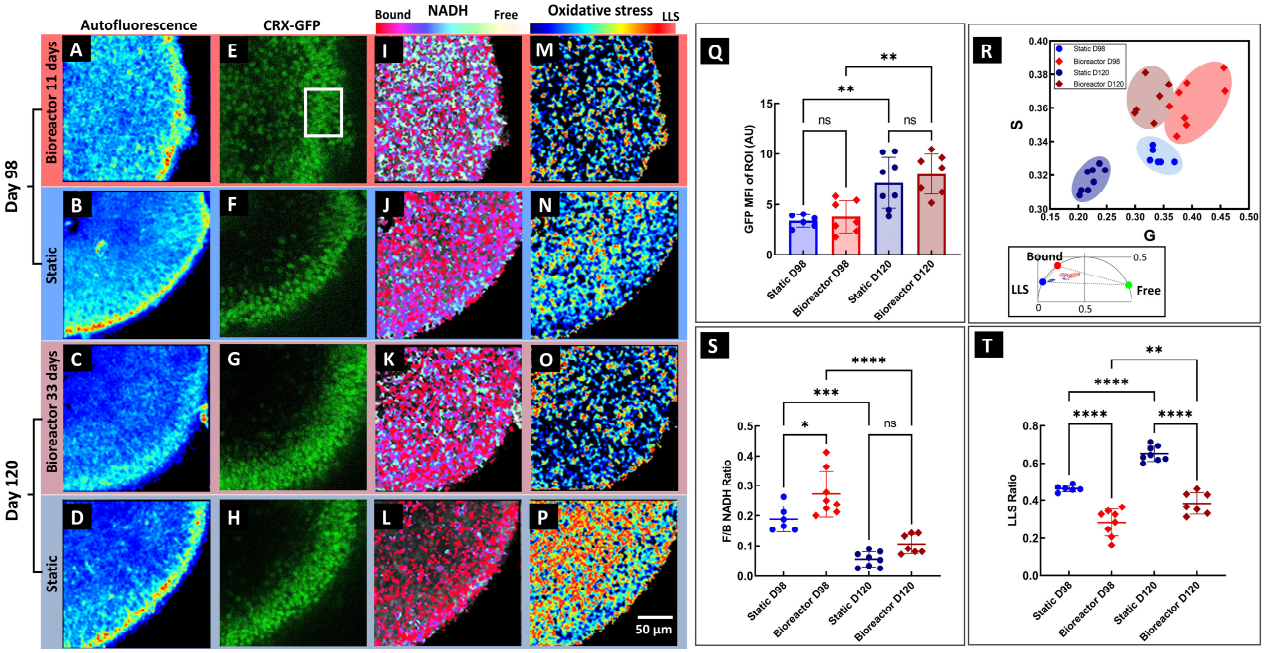

Figure 7: Qualitative and quantitative comparison of RtOgs in two culture methods. (A-D) Total NADH autofluorescence images showed the cellular structures within the RtOgs' cross section; (E-H) Fluorescence images showed distinct cell nuclear layer corresponding to the CRX-GFP fusion protein localized in nuclei; (I-L) Pseudo color-coded free/bound NADH distribution and (M-P) LLS distribution images were generated based on photon lifetime locations within the 2-dminensional phasor space; (Q) The mean fluorescence intensity of GFP signals at region of interest (white box in Fig. 7E) (One-way ANOVA test was performed: Static D98, n = 6; Bioreactor D98, n = 7; Static D120 n = 8; Bioreactor D120, n = 7); (R) Scatter plot of imaged RtOgs and their location on the FLIM phasor diagram; (S) Plot of free/bound NADH ratio to evaluate metabolism (higher f/b value represented glycolysis, and lower f/b indicated greater oxidative phosphorylation; (T) Plot of LLS ratio to evaluate oxidative stress. (One-way ANOVA test was performed: Static D98, n = 6; Bioreactor D98, n = 8; Static D120 n = 8; Bioreactor D120, n = 7).

Gene expression profile

We also examined the RtOgs' gene expression by fluorescence imaging and qPCR analysis. RtOgs in both groups displayed a thick nuclear outer layer which expressed CRX gene on day 120 of differentiation (Figs. 7E-H). The mean fluorescent intensity (MFI) of the selected outer surface region showed no significant difference between static and bioreactor cultured RtOgs on day 98 and 120. However, both groups had a significant increase of MFI over time, which suggests an increase of CRX expression during RtOgs differentiation (Fig. 7Q).

The qPCR test provided a comprehensive retina related gene profile. Fig. 8A showed that both groups expressed retinal progenitor genes (CHX10, NRL and RAX) that were comparable to those of human adult retina. Both groups also expressed rod and cone genes including RCVRN, ARR3, SAG, PRPH2, GNAT and GNAT2. However, both groups had very little mature photoreceptor gene expression, which was expected, as RtOgs typically do not reach full maturity until day 150~200 of differentiation. The gene expression level showed no significant difference between static group and RtOgs group (two-way ANOVA test, $p>0.05$). However, RtOgs on the bioreactor expressed more OPN1 MW than static group ($p=0.0633$), which implied that micro-millifluidic bioreactor might be the optimal platform for photoreceptor maturation.

Hematoxylin-eosin staining

Lastly, the RtOgs maintained in both conventional static culture or the bioreactor were fixed on day 124 of differentiation and frozen sectioning performed to acquire hematoxylin and eosin (H&E) cross-sections. Representative images are shown in Figs. 8B-E. RtOgs in both groups demonstrated clear and compact outer nuclear layer on the organoids surface, which suggested the formation of photoreceptor layer. RtOgs maintained in conventional culture demonstrated lacy vacuolization of the inner tissues, whereas the same was not as prominent in the bioreactor-maintained organoids.

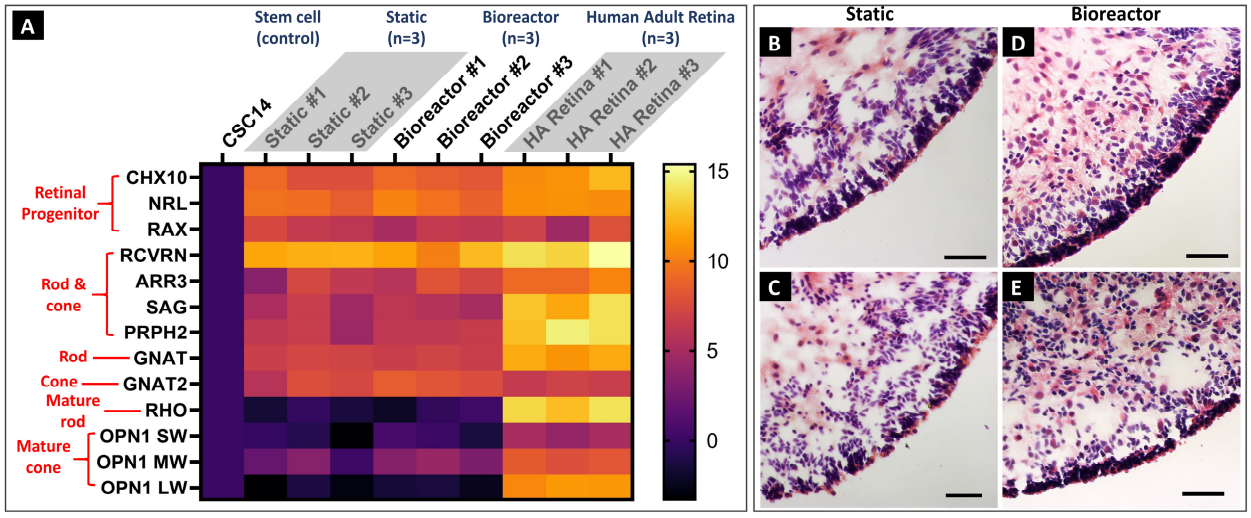

Figure 8: Gene profile and representative histology images of different experimental groups. (A) The CSC14 stem cell was used as negative control and calibrator for all other groups. Each sample in each experimental group contained 4 RtOgs. The human adult (HA) retina samples were set as positive controls. (B) Four Representative RtOgs in static culture (B-C) and bioreactor culture (D-E) on day 124 of differentiation (scale bar: 50 μm).

DISCUSSION

The overall goal of this study was to improve current RtOgs culture techniques by reducing manual labor required for organoid culture and improve the RtOgs reproducibility and quality. Two main differences between *in vivo* retina and conventional *in vitro* RtOg culture: consistency of nutrition supply and fluid mechanical stability. In the human body, the visual system is the highest energy-consuming system in the brain [51] and photoreceptor cells are identified as the most metabolically active cell. Retinas in the human body are continuously nourished by the dual blood supply from the choriocapillaris and the retinal vasculature. Additionally, the retina *in vivo* is isolated from mechanical forces, by virtue of the non-compressible fluid contents for the globe and the outermost structural support provided by the sclera. In its natural configuration, the photoreceptors are isolated from dynamic fluid forces, whereas organoids in tissue culture

develop photoreceptors surrounded by turbulence in multi-well culture plates. Shear stress can impact the stem cell differentiation phenotypes [52], destroy circulating tumor cells [53], induce cells' metabolite production [54], and cause RtOgs to lose the outer segment like structures [55]. Loss of photoreceptor outer segments is also seen clinically in patients with retinal detachments who develop glaucoma as a consequence of outer segment shedding [56].

Bioreactors for organoid culture to remedy the drawbacks of conventional tissue culture have been described in recent years. Existing challenges for bioreactor designs include minimizing the volume of media used, minimizing shear stresses on tissues and reducing their incompatibility with longitudinal non-invasive imaging. At the macro level, stirred and rotating wall vessel (RWV) platforms have been used for retinal organoid differentiation. The former has been shown to produce retinal organoids with improved laminar stratification and increased yield of photoreceptor cells with outer segment structure, with drawbacks of damage to these fragile structures from sheer stress [55]. The latter has the advantages of improved differentiation, easy use, and high nutrient transfer, and has also been used to culture bladder, lung, intestinal, and vaginal epithelial cell types into three-dimensional cell aggregates [31], [57-60]. However, these larger systems share the disadvantage of high cost due to the high volume of media required to maintain the organoids [34]. At an intermediate scale is the millifluidic system used to manipulate fluids for organoid maintenance [36]. These bioreactors have been used for development of kidney organoids and long-term maintenance of human midbrain and liver organoids [29, 61, 62]. Millifluidic systems have the advantages of supporting relatively high flow rates, cell-cell interaction, and less frequent media changes and thus less organoid perturbation but has the disadvantage of intermediately high volume and cost, and low throughput. At the microscale, microfluidic devices have the added advantages of lower volume and lower cost compare to millifluidics [36]. Microfluidic devices have been used to culture human intestinal, lung, hepatocyte, and cardiac organoids, [63-65]. For both the milli- and microfluidic devices, shear stress can be minimized by placing organoids in wells or

chambers at a set distance from the flow channels. Therefore, we sought to reduce shear stress while creating a perfused environment to house and isolate individual organoids for long term non-invasive imaging.

First, we developed a hybrid bioreactor design that incorporated both micro and milifluidic components. This design was made possible from the novel fabrication method relying on SLA 3D printers to create a mold incorporating micro-, milli- and even macroscopic features (Figs. 2A-D). Thanks to the development of additive manufacturing techniques, we were able to utilize the SLA 3D printing to combine the micro and milli features easily in one single design. 3D printing also enabled rapid prototyping bioreactor designs to iteratively optimize the design. Cost savings and facility compared with traditional microfabrication methods offers additive manufacturing as a useful approach to manufacturing bioreactors [66].

We used computer simulation to first demonstrate that each millifluidic culture chamber could be supplied with media from a microfluidic channel. We evaluated flow velocity inside culture chambers and found no active flow (Fig. 4C), which satisfied the design goals to minimize turbulence and shear stresses on retinal organoids by eliminating fluidic movement in the culture chamber. We further optimized channel geometry relative to the culture chambers, flow rate of media through the bioreactor and inclusion of microfluidic mixers between each culture chamber. The endpoint for determining success in each design iteration was comparing uniformity of media composition in each culture chamber. We performed both COMSOL simulations *in silico* (Fig. 4) as well as dye tests *in vitro* (Fig. 5). *In silico* simulations demonstrated that narrow microfluidic channels (500 μm wide x 200 μm tall) allowed greater mass transfer than wider microfluidic channels (1 mm wide x 200 μm tall). We also observed *in silico* that high flow rate (250 vs 600 μL/hr) also improved mass transfer into culture chambers (Fig. 4B). *In vitro* dye tests to confirm *in silico* modeling predictably revealed that bioreactor designs with all culture chambers arranged on the same side of the microfluidic channel suffered from diffusion from a single side of the

channels laminar flow. This resulted in the first chamber in each row of the microfluidic series to have the highest mass transfer of fresh media, while the last chamber had the lowest (Fig. 5A). To overcome this limitation, we designed a bioreactor with serpentine microfluidic flow line and culture chambers on alternating sides of the microfluidic flow line. These designs were simulated *in silico* to reveal improved concentration uniformity in each culture chamber compared with straight channel designs. *In vitro* dye testing confirmed that media concentration variability between all wells was improved by the serpentine design (Fig. 5B). Finally, we introduced mixers in the flow channel to determine if mixing would improve culture chamber concentration uniformity. *In silico* simulation demonstrated improved chamber concentration uniformity over the serpentine channel design (Fig. 5A). *In vitro* dye testing demonstrated a marginal improvement when the mixer was included than when it was not. A decision based on practical implementation was made to exclude the mixer because of the higher probability of trapping bubbles in the mixer elements as well as the mixer having tapered features that exceeded the resolution of the 3D printers employed.

A second major requirement for our design was to enable long-term imaging of retinal organoids maintained in perfused culture. The bioreactor chip design included glass cover slips to seal the microfluidic circuit. Glass cover slips are thinner than microscope slides and, therefore, suitable for both multiphoton imaging and conventional fluorescence microscopy. Multiphoton imaging relies upon optimally efficient photon capture, and thicker glass slide reduces captured photons below threshold of practical imaging.

Archberger *et al*. demonstrated a chip platform containing tissue chambers seeded with RPE and fed with media via a porous membrane to mimic vasculature in the retina [67]. This platform emphasized human physiological fidelity and minimized shear stress. However, a limitation was the relatively short 7-day maintenance of the chip platform for organoid culture. After optimizing our bioreactor design, we evaluated its performance in sustaining retinal organoids. The protocol

493 for loading organoids into the bioreactor was determined as described in Figs. 2E-F. In this body
494 of work we sought to evaluate the bioreactor's ability to maintain RtOgs for 1 month. We
495 compared organoids differentiated to 88 days *in vitro* that were either placed in the bioreactor for
496 37 days or remained in conventional plate culture. Non-invasive functional imaging of metabolism
497 and oxidative stress, sustained development of photoreceptors on the organoids outer layer, and
498 terminal PCR analysis of RtOg tissue were endpoints for comparing culture conditions. Phase
499 contrast microscopy revealed that RtOgs maintained in conventional culture and bioreactors
500 developed a comparable semi-translucent outer layer. Qualitatively, we observed slightly more
501 photoreceptor outer segments in the RtOgs maintained in the bioreactor. The fluorescent reporter
502 GFP linked to nuclear CRX served as a marker for photoreceptors and their progenitors. We
503 observed an insignificant difference in the fluorescence intensity of GFP^+ nuclei in organoids of
504 the same age when they were cultured in the bioreactor or conventional culture (Fig. 7Q),
505 suggesting the cellular composition is likely similar between RtOgs maintained in either culture
506 condition.

507 However, we observed a statistically significant difference in metabolism and oxidative stress
508 between organoids maintained in the bioreactor versus conventional culture (Fig. 7). Organoids
509 in the bioreactor had significantly higher total NADH signal. It is worth noting that bioreactor
510 cultured RtOgs at both timepoints presented similar f/b NADH ratio as those in static culture,
511 indicating similar differentiated state [68] (Fig. 7S), but the total NADH signal was lower in organoids
512 maintained in conventional culture. Furthermore, organoids in the bioreactor demonstrated lower
513 LLS levels suggesting that they experience less oxidative stress than organoids maintained in
514 conventional tissue culture (Fig. 7T). We confirmed with gene expression for retinal genes and
515 observed no significant difference between RtOgs maintained in conventional culture or the
516 bioreactor (Fig. 8A). Because RtOgs expressed similar gene expression profiles after 37 days of
517 on-chip culture to human adult retina, this is promising for future observations optimization to
518 develop mature retinal without segment structures (SFig. 2), which are typically observed under

519 long term culture conditions [69]. H&E staining of organoids maintained in the bioreactor or in
520 conventional culture suggested a possible difference in tissue architecture between the two
521 groups. RtOgs maintained in culture may have greater propensity for vacuole formation that
522 correlates anatomically with a greater LLS and oxidative stress (Fig. 8B-E).
523

524 **CONCLUSION**

525 In this study, we designed and optimized a bioreactor for long term RtOg culture in a low
526 shear stress environment that was also compatible with multimodal imaging. We found that
527 higher flow rates through narrower channels with culture chambers on alternating sides of the
528 perfusion channel enabled optimal and practical concentration uniformity between culture
529 chambers. We subsequently achieved RtOgs culture on a shear stress-free micro-millifluidic
530 bioreactor for 1 month and identified key similarities and differences between RtOgs maintained
531 in either static culture or the bioreactor. We found that: 1) bioreactor cultured RtOgs developed
532 transparent layered surface structure comparable to static cultured ones; 2) the outer surface
533 region of bioreactor cultured RtOgs had comparable free/bound NADH ratio and overall lower
534 long lifetime species (LLS) ratio than static culture RtOgs; 3) RtOgs maintained for 22 days in
535 either the bioreactor or conventional culture expressed significantly higher CRX than that on day
536 98; and 4), there was no significant difference in gene expression between static conventional
537 culture and bioreactor culture. Therefore, the micro-millifluidic bioreactor in this study has
538 demonstrated its potential to sustain RtOgs of equal or better quality than organoids maintained
539 in static culture, while achieving this goal in a low maintenance, sheer stress-free system.
540

541 **AUTHOR CONTRIBUTIONS**

542 Y.X.: methodology, data curation, formal analysis, investigation, visualization and writing of
543 original draft; M.S.: funding acquisition, project administration, resources, supervision, validation

and manuscript review & editing; W.T.: conceptualization, project administration, supervision, validation and manuscript review & editing ; J.W.: investigation, visualization and writing of original draft; A.B.: conceptualization, funding acquisition, methodology, project administration, resources, supervision, validation, visualization, manuscript review & editing.

CONFLICTS OF INTEREST

There are no conflicts to declare.

ACKNOWLEDGEMENTS

This work was supported by CIRM (#TRAN1-10995), RPB unrestricted grant to UCI Department of Ophthalmology and ICTS KL2 (#KL2 TR001416). We thank Dr. Majlinda Lako (Newcastle University, UK.) for donating the CRX GFP hESC cell line, Drs. Michelle Digman (Dept. of BME, UCI) and Enrico Gratton (Dept. of BME, UCI) for their help and advice on fluorescence lifetime imaging, and Bryce McLelland (AIVITA Biomedical Inc, California) for instructions on retinal organoids initiation. We thank the Optical Biology Center in UCI for providing microscopic facilities and Stem Cell Research Center Core for qPCR and histology service. We also thank all the undergraduate students that participated in this project: Johnny Garcia (now B.S.), Yuming Ye, Xiyue Yao, Lelin Zhong, Vanna Giang and Mojan Rouhizadeh.

REFERENCES

1. M. J. Seiler, R. B. Aramant and S. L. Ball, *Vision Res*, 1999, **39**, 2589-2596.
2. G. Woch, R. B. Aramant, M. J. Seiler, B. T. Sagdullaev and M. A. McCall, *Invest Ophthalmol Vis Sci*, 2001, **42**, 1669-1676.
3. B. T. Sagdullaev, R. B. Aramant, M. J. Seiler, G. Woch and M. A. McCall, *Invest Ophthalmol Vis Sci*, 2003, **44**, 1686-1695.

4. B. B. Thomas, M. J. Seiler, S. R. Sadda and R. B. Aramant, *Exp Eye Res*, 2004, **79**, 29-39.
5. P. B. Yang, M. J. Seiler, R. B. Aramant, F. Yan, M. J. Mahoney, L. M. Kitzes and H. S. Keirstead, *Exp Eye Res*, 2010, **91**, 727-738.
6. M. J. Seiler, R. E. Lin, B. T. McLelland, A. Mathur, B. Lin, J. Sigman, A. T. De Guzman, L. M. Kitzes, R. B. Aramant and B. B. Thomas, *Invest Ophthalmol Vis Sci*, 2017, **58**, 614-630.
7. B. B. Thomas, R. B. Aramant, S. R. Sadda and M. J. Seiler, in *Retinal Degenerative Diseases*, eds. J. G. Hollyfield, R. E. Anderson and M. M. LaVail, Springer, New York, NY, 2006, pp. 367-376.
8. R. B. Aramant and M. J. Seiler, *Prog Retin Eye Res*, 2004, **23**, 475-494.
9. M. J. Seiler, R. B. Aramant and H. S. Keirstead, *Optics and Photonics News*, 2008, **19**, 37-47.
10. M. J. Seiler and R. B. Aramant, *Prog Retin Eye Res*, 2012, **31**, 661-687.
11. N. D. Radtke, R. B. Aramant, H. M. Petry, P. T. Green, D. J. Pidwell and M. J. Seiler, *Am J Ophthalmol*, 2008, **146**, 172-182.
12. B. A. Tucker, I. H. Park, S. D. Qi, H. J. Klassen, C. Jiang, J. Yao, S. Redenti, G. Q. Daley and M. J. Young, *PLoS ONE*, 2011, **6**, e18992.
13. R. A. Pearson, A. C. Barber, M. Rizzi, C. Hippert, T. Xue, E. L. West, Y. Duran, A. J. Smith, J. Z. Chuang, S. A. Azam, U. F. Luhmann, A. Benucci, C. H. Sung, J. W. Bainbridge, M. Carandini, K. W. Yau, J. C. Sowden and R. R. Ali, *Nature*, 2012, **485**, 99-103.
14. M. S. Singh, P. Charbel Issa, R. Butler, C. Martin, D. M. Lipinski, S. Sekaran, A. R. Barnard and R. E. MacLaren, *Proc Natl Acad Sci U S A*, 2013, **110**, 1101-1106.
15. D. A. Lamba, J. Gust and T. A. Reh, *Cell Stem Cell*, 2009, **4**, 73-79.
16. R. E. MacLaren, R. A. Pearson, A. MacNeil, R. H. Douglas, T. E. Salt, M. Akimoto, A. Swaroop, J. C. Sowden and R. R. Ali, *Nature*, 2006, **444**, 203-207.
17. F. C. Mansergh, R. Vawda, S. Millington-Ward, P. F. Kenna, J. Haas, C. Gallagher, J. H. Wilson, P. Humphries, M. Ader and G. J. Farrar, *Exp Eye Res*, 2010, **91**, 500-512.
18. J. A. Thomson, J. Itskovitz-Eldor, S. S. Shapiro, M. A. Waknitz, J. J. Swiergiel, V. S. Marshall and J. M. Jones, *science*, 1998, **282**, 1145-1147.
19. K. Takahashi, K. Tanabe, M. Ohnuki, M. Narita, T. Ichisaka, K. Tomoda and S. Yamanaka, *Cell*, 2007, **131**, 861-872.
20. C. M. Fligor, K. B. Langer, A. Sridhar, Y. Ren, P. K. Shields, M. C. Edler, S. K. Ohlemacher, V. M. Sluch, D. J. Zack and C. Zhang, *Scientific reports*, 2018, **8**, 14520.
21. K. Wahlin, J. Maruotti, S. Sripathi, J. Ball, J. Angueyra, C. Kim, R. Grebe, W. Li, B. Jones and D. Zack, *Journal*, 2017.
22. T. Nakano, S. Ando, N. Takata, M. Kawada, K. Muguruma, K. Sekiguchi, K. Saito, S. Yonemura, M. Eiraku and Y. Sasai, *Cell Stem Cell*, 2012, **10**, 771-785.
23. B. T. McLelland, B. Lin, A. Mathur, R. B. Aramant, B. B. Thomas, G. Nistor, H. S. Keirstead and M. J. Seiler, *Investigative ophthalmology & visual science*, 2018, **59**, 2586-2603.
24. J. Assawachananont, M. Mandai, S. Okamoto, C. Yamada, M. Eiraku, S. Yonemura, Y. Sasai and M. Takahashi, *Stem cell reports*, 2014, **2**, 662-674.
25. H. Shirai, M. Mandai, K. Matsushita, A. Kuwahara, S. Yonemura, T. Nakano, J. Assawachananont, T. Kimura, K. Saito and H. Terasaki, *Proceedings of the National Academy of Sciences*, 2016, **113**, E81-E90.
26. S. Llonch, M. Carido and M. Ader, *Dev Biol*, 2018, **433**, 132-143.
27. C. B. Mellough, J. Collin, R. Queen, G. Hilgen, B. Dorgau, D. Zerti, M. Felemban, K. White, E. Sernagor and M. Lako, *Stem cells translational medicine*, 2019, **8**, 694-706.

28. Z. Ao, H. Cai, D. J. Havert, Z. Wu, Z. Gong, J. M. Beggs, K. Mackie and F. Guo, *Anal Chem*, 2020, **92**, 4630-4638.
29. E. Berger, C. Magliaro, N. Paczia, A. S. Monzel, P. Antony, C. L. Linster, S. Bolognin, A. Ahluwalia and J. C. Schwamborn, *Lab Chip*, 2018, **18**, 3172-3183.
30. M. E. Boutin, C. Hampton, R. Quinn, M. Ferrer and M. J. Song, *Adv Exp Med Biol*, 2019, **1186**, 171-193.
31. T. DiStefano, H. Y. Chen, C. Panebianco, K. D. Kaya, M. J. Brooks, L. Gieser, N. Y. Morgan, T. Pohida and A. Swaroop, *Stem cell reports*, 2018, **10**, 300-313.
32. L. Goto-Silva, N. M. E. Ayad, I. L. Herzog, N. P. Silva, B. Lamien, H. R. B. Orlande, A. da Costa Souza, S. Ribeiro, M. Martins, G. B. Domont, M. Junqueira, F. Tovar-Moll and S. K. Rehen, *BMC Dev Biol*, 2019, **19**, 3.
33. P. Ovando-Roche, E. L. West, M. J. Branch, R. D. Sampson, M. Fernando, P. Munro, A. Georgiadis, M. Rizzi, M. Kloc, A. Naeem, J. Ribeiro, A. J. Smith, A. Gonzalez-Cordero and R. R. Ali, *Stem Cell Res Ther*, 2018, **9**, 156.
34. M. A. Phelan, P. I. Lelkes and A. Swaroop, *Stem Cell Investig*, 2018, **5**, 33.
35. A. Artero Castro, F. J. Rodriguez Jimenez, P. Jendelova and S. Erceg, *Stem Cells*, 2019, **37**, 1496-1504.
36. M. J. Beauchamp, G. P. Nordin and A. T. Woolley, *Anal Bioanal Chem*, 2017, **409**, 4311-4319.
37. D. Smith, et al. , 2014.
38. E. Berger, C. Magliaro, N. Paczia, A. S. Monzel, P. Antony, C. L. Linster, S. Bolognin, A. Ahluwalia and J. C. Schwamborn, *Lab on a Chip*, 2018, **18**, 3172-3183.
39. B. Sidar, B. R. Jenkins, S. Huang, J. R. Spence, S. T. Walk and J. N. Wilking, *Lab Chip*, 2019, **19**, 3552-3562.
40. D. Qin, Y. Xia and G. M. Whitesides, *Nature protocols*, 2010, **5**, 491-502.
41. J. Collin, C. B. Mellough, B. Dorgau, S. Przyborski, I. Moreno-Gimeno and M. Lako, *Stem Cells*, 2016, **34**, 311-321.
42. X. Zhong, C. Gutierrez, T. Xue, C. Hampton, M. N. Vergara, L.-H. Cao, A. Peters, T. S. Park, E. T. Zambidis and J. S. Meyer, *Nature communications*, 2014, **5**, 4047.
43. M. A. Digman, V. R. Caiolfa, M. Zamai and E. Gratton, *Biophys J*, 2008, **94**, L14-16.
44. S. Ranjit‡, L. Malacrida‡, M. Stakic and E. Gratton.
45. C. Stringari, J. L. Nourse, L. A. Flanagan and E. Gratton, *PloS one*, 2012, **7**, e48014.
46. R. Datta, A. Alfonso-García, R. Cinco and E. Gratton, *Sci Rep*, 2015, **5**, 9848.
47. C.-C. Hong, J.-W. Choi and C. H. Ahn, *Lab on a Chip*, 2004, **4**, 109-113.
48. A. W. Browne, C. Arnesano, N. Harutyunyan, T. Khuu, J. C. Martinez, H. A. Pollack, D. S. Koos, T. C. Lee, S. E. Fraser, R. A. Moats, J. G. Aparicio and D. Cobrinik, *Invest Ophthalmol Vis Sci*, 2017, **58**, 3311-3318.
49. C. Stringari, R. A. Edwards, K. T. Pate, M. L. Waterman, P. J. Donovan and E. Gratton, *Scientific reports*, 2012, **2**, 1-9.
50. B. K. Wright, L. M. Andrews, J. Markham, M. R. Jones, C. Stringari, M. A. Digman and E. Gratton, *Biophysical journal*, 2012, **103**, L7-L9.
51. J. E. Niven and S. B. Laughlin, *The Journal of experimental biology*, 2008, **211**, 1792-1804.
52. R. P. Wolfe and T. Ahsan, *Biotechnology and bioengineering*, 2013, **110**, 1231-1242.
53. S. Regmi, A. Fu and K. Q. Luo, *Scientific Reports*, 2017, **7**, 39975.
54. J. A. Frangos, L. V. McIntire and S. G. Eskin, *Biotechnology and bioengineering*, 1988, **32**, 1053-1060.
55. P. Ovando-Roche, E. L. West, M. J. Branch, R. D. Sampson, M. Fernando, P. Munro, A. Georgiadis, M. Rizzi, M. Kloc, A. Naeem, J. Ribeiro, A. J. Smith, A. Gonzalez-Cordero and R. R. Ali, *Stem Cell Research & Therapy*, 2018, **9**, 156.
56. A. Schwartz, *Transactions of the American Ophthalmological Society*, 1972, **70**, 178.

57. Y. C. Smith, Grande, K. K., Rasmussen, S. B., & O'Brien, A. D., 2006.
58. A. J. Carterson, Höner zu Bentrup, K., Ott, C. M., Clarke, M. S., Pierson, D. L., Vanderburg, C. R., Buchanan, K. L., Nickerson, C. A., Schurr, M. J., *Infection and Immunity*, 2005, **73**, 1129-1140.
59. R. Salerno-Goncalves, A. Fasano and M. B. Sztein, *J Vis Exp*, 2016, DOI: 10.3791/54148.
60. B. E. Hjelm, A. N. Berta, C. A. Nickerson, C. J. Arntzen and M. M. Herbst-Kralovetz, *Biol Reprod*, 2010, **82**, 617-627.
61. K. A. Homan, N. Gupta, K. T. Kroll, D. B. Kolesky, M. Skylar-Scott, T. Miyoshi, D. Mau, M. T. Valerius, T. Ferrante, J. V. Bonventre, J. A. Lewis and R. Morizane, *Nat Methods*, 2019, **16**, 255-262.
62. S. D. Ramachandran, K. Schirmer, B. Munst, S. Heinz, S. Ghafoory, S. Wolfl, K. Simon-Keller, A. Marx, C. I. Oie, M. P. Ebert, H. Walles, J. Braspenning and K. Breitkopf-Heinlein, *PLoS One*, 2015, **10**, e0139345.
63. M. Kasendra, A. Tovaglieri, A. Sontheimer-Phelps, S. Jalili-Firoozinezhad, A. Bein, A. Chalkiadaki, W. Scholl, C. Zhang, H. Rickner, C. A. Richmond, H. Li, D. T. Breault and D. E. Ingber, *Sci Rep*, 2018, **8**, 2871.
64. Y. S. Zhang, J. Aleman, S. R. Shin, T. Kilic, D. Kim, S. A. Mousavi Shaegh, S. Massa, R. Riahi, S. Chae, N. Hu, H. Avci, W. Zhang, A. Silvestri, A. Sanati Nezhad, A. Manbohi, F. De Ferrari, A. Polini, G. Calzone, N. Shaikh, P. Alerasool, E. Budina, J. Kang, N. Bhise, J. Ribas, A. Pourmand, A. Skardal, T. Shupe, C. E. Bishop, M. R. Dokmeci, A. Atala and A. Khademhosseini, *Proc Natl Acad Sci U S A*, 2017, **114**, E2293-E2302.
65. G. Mattei, Giusti, Serena, Ahluwalia, Arti, 2014, **2**, 548-569.
66. N. P. Macdonald, J. M. Cabot, P. Smejkal, R. M. Guijt, B. Paull and M. C. Breadmore, *Analytical Chemistry*, 2017, **89**, 3858-3866.
67. K. P. Archberger, C.; Haderspeck, J.; Bolz, S.; Rogal, J.; Chuchuy, J.; Nikolova, M.; Cora, V.; Antowiak, L.; Haq, W.; Shen, N.; Schenke-Layland, K.; Ueffing, M.; Liebau, S.; Loskill, P. , *eLife* 2019, DOI: 10.7554/eLife.46188.
68. R. Datta, C. Heylman, S. C. George and E. Gratton, *Biomedical optics express*, 2016, **7**, 1690-1701.
69. K. Achberger, J. C. Haderspeck, A. Kleger and S. Liebau, *Adv Drug Deliv Rev*, 2019, **140**, 33-50.